*pharmaceutics*

MDPI

*Article*

# Selective Anticancer Therapy Based on a HA-CD44 Interaction Inhibitor Loaded on Polymeric Nanoparticles

**José M. Espejo-Román [1,2,3], Belén Rubio-Ruiz [1,2,3], Victoria Cano-Cortés [1,2,3], Olga Cruz-López [1,3], Saúl Gonzalez-Resines [4], Carmen Domene [4,5], Ana Conejo-García [1,3,*] and Rosario M. Sánchez-Martín [1,2,3,*]**

1 Department of Medicinal and Organic Chemistry and Excellence Research Unit of Chemistry Applied to Biomedicine and the Environment, Faculty of Pharmacy, Campus Cartuja s/n, University of Granada, 18071 Granada, Spain; jmespejo@ugr.es (J.M.E.-R.); belenrubio@ugr.es (B.R.-R.); vccortes@go.ugr.es (V.C.-C.); olgacl@ugr.es (O.C.-L.)
2 GENYO, Centre for Genomics and Oncological Research, Pfizer/University of Granada/Andalusian Regional Government, PTS Granada, Avda. Ilustración 114, 18016 Granada, Spain
3 Biosanitary Institute of Granada (ibs.GRANADA), SAS-University of Granada, Avenida de Madrid, 15, 18012 Granada, Spain
4 Department of Chemistry, University of Bath, Claverton Down, Bath BA2 7AX, UK; s.gonzalez.resines@bath.ac.uk (S.G.-R.); mcdn20@bath.ac.uk (C.D.)
5 Chemistry Research Laboratory, University of Oxford, Mansfield Road, Oxford OX1 3TA, UK
* Correspondence: aconejo@ugr.es (A.C.-G.); rmsanchez@ugr.es (R.M.S.-M.)

**Abstract:** Hyaluronic acid (HA), through its interactions with the cluster of differentiation 44 (CD44), acts as a potent modulator of the tumor microenvironment, creating a wide range of extracellular stimuli for tumor growth, angiogenesis, invasion, and metastasis. An innovative antitumor treatment strategy based on the development of a nanodevice for selective release of an inhibitor of the HA-CD44 interaction is presented. Computational analysis was performed to evaluate the interaction of the designed tetrahydroisoquinoline-ketone derivative (**JE22**) with CD44 binding site. Cell viability, efficiency, and selectivity of drug release under acidic conditions together with CD44 binding capacity, effect on cell migration, and apoptotic activity were successfully evaluated. Remarkably, the conjugation of this CD44 inhibitor to the nanodevice generated a reduction of the dosis required to achieve a significant therapeutic effect.

**Keywords:** nanomedicine; selective release; anticancer therapy; hyaluronic acid; cluster of differentiation 44; tetrahydroisoquinoline; molecular dynamics simulations



**Citation:** Espejo-Román, J.M.; Rubio-Ruiz, B.; Cano-Cortés, V.; Cruz-López, O.; Gonzalez-Resines, S.; Domene, C.; Conejo-García, A.; Sánchez-Martín, R.M. Selective Anticancer Therapy Based on a HA-CD44 Interaction Inhibitor Loaded on Polymeric Nanoparticles. *Pharmaceutics* **2022**, *14*, 788. https://doi.org/10.3390/pharmaceutics14040788

Academic Editors: Maria Carmo Pereira and Maria João Ramalho

Received: 6 March 2022
Accepted: 1 April 2022
Published: 4 April 2022



## 1. Introduction

Hyaluronic acid or hyaluronan (HA), the main component of the extracellular matrix, is a linear polysaccharide composed of repeating disaccharide units of *N*-acetyl-D-glucosamine and D-glucuronic acid with β-(1→4) interglycosidic linkages. In normal physiological conditions, the number of repeating disaccharides in an HA molecule ranges from 2000 to 25,000, resulting in a viscose and elastic solution with a large hydrodynamic volume that helps to maintain tissue integrity and homeostasis [1].

Besides its key role as structural component of tissues, HA is also involved in multiple signaling pathways, under both physiological (embryogenesis) and pathological conditions such as inflammation or cancer [2,3]. This unique biological function is attributed to its specific binding and interactions with HA-binding proteins, termed hyaladherins, which comprise several types of cell-surface receptors. Of these, cluster of differentiation 44 (CD44), a signal-transducing glycoprotein, is the major surface HA receptor, which is implicated in a variety of cellular events such as cell proliferation, differentiation, migration, and angiogenesis [4,5]. There is clear evidence that extensive HA production due to an aberrant synthesis or turnover occurs during malignant transformation. These abnormal HA levels are strongly associated with tumor aggressiveness and a fatal disease outcome.

Likewise, the expression of CD44 is elevated in many types of malignancies compared to CD44 levels in the corresponding healthy tissues. Pathological conditions also promote alternate splicing and post-translational modifications, resulting in diversified CD44 molecules with enhanced HA binding leading to increased tumorigenicity [6,7]. Thus, HA acts as a potent modulator of tumor microenvironments through its interactions with CD44. Consequently, targeting the interactions between HA and CD44 is a promising approach against HA-induced tumorigenesis.

Nanotechnology has made a remarkable contribution to cancer diagnosis and, importantly, cancer therapy [8,9]. In order to provide more effective and safer treatments, several nanodevices targeting CD44 receptors have been reported to specifically carry and deliver drugs [10–13]. The design of these nanosystems is based on the use of HA as the ligand for selective delivery of therapy on tumor cells overexpressing CD44. Moreover, a novel strategy has been recently reported using anti-CD44 antibody as the ligand for selective delivery of paclitaxel for treatment of pancreatic cancer [14]. However, a nanotechnology-based strategy for the inhibition of CD44 receptors as an anticancer therapeutic approach has not been reported so far.

Crystal structure analysis together with mutagenesis studies of both murine and human CD44 have pinpointed the essential residues for HA binding to CD44 [15,16]. The CD44 HA-binding domain (CD44 HABD) is in the N-terminal domain at the extracellular region of the receptor. By means of biophysical binding assays, fragment screening, and crystallographic characterization of complexes with CD44 HABD, Liu LK et al. discovered an inducible pocket adjacent to the HA-binding groove in which small tetrahydroisoquinoline (THIQ)-containing molecules bind [16]. Among them, the **THIQ-ester** derivative (Figure 1) showed a significant affinity for the isolated protein.

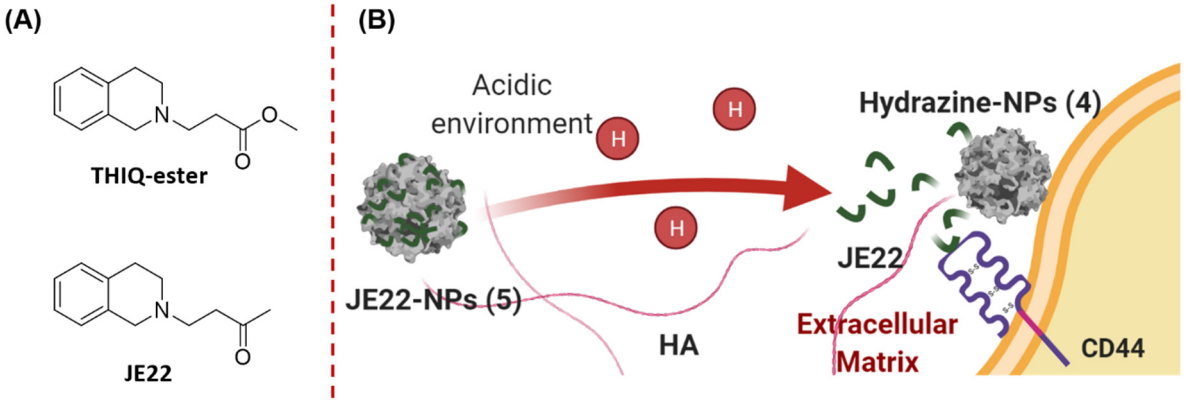


**Figure 1.** Schematic overview of the strategy proposed. (**A**) Chemical structures of the CD44 inhibitors. (**B**) Specific release of the THIQ inhibitor **JE22** bound to the nanodevice **JE22-NPs** (**5**) as a result of the acidic environment in the cancer cells, and subsequent therapeutic activity by its binding to CD44.

Based on our broad expertise in the functionalization of nanoparticles for the selective delivery of biomolecules [17–22], our aim was to implement a nanotechnology strategy to enhance the efficiency of the THIQ derivatives targeting CD44 to achieve a potential antitumor treatment. We first designed and synthesized an analogue of the reported CD44 inhibitor (**THIQ-ester**, Figure 1) [16] by replacement of the ester functional group by a ketone (**JE22**, Figure 1) to allow for the conjugation to the nanospheres via the hydrazone bond. This nanodevice **JE22-NPs** (**5**) selectively releases this THIQ derivative as a specific inhibitor of the HA–CD44 interaction at the acidic tumor microenvironment (Figure 1).

## 2. Materials and Methods

### *2.1. Computational*

#### 2.1.1. Systems Set Up

The crystal structure of the murine CD44 HABD at 1.4 Å resolution (PDB ID: 5BZK) [16] was used as a starting point for the computational work. The protein was inserted in a water box of 90 × 90 × 90 $A^3$ dimensions, and KCl was added up to a final concentration of 150 mM using the CHARMM-GUI Solution Builder server [23–26]. Two independent systems were built with the **THIQ-ester** and **JE22** ligands, respectively. The **JE22** molecule was aligned using the position of the **THIQ-ester** ligand present in PDB id 5BZK. The final systems were composed of ~66,000 atoms. Five different replicas were run for each system.

#### 2.1.2. Molecular Dynamics Simulations

The CHARMM36 force field [27,28] was used to model the protein, standard CHARMM parameters were used for ions, and the TIP3P model for water [29]. The charges and parameters for the ligands were searched using the CHARMM-GUI ligand modeler interface [30,31] that generates the ligand force field parameters and necessary structure files by inspecting small molecules in the verified CHARMM force field library or using the CHARMM general force field (CGenFF) [32]. The results suggested optimizing the charges and certain dihedral angles as the penalties were high. Geometry, charge, and dihedral optimization were performed for the two ligands following a standard protocol described in the Supplementary Materials (Scheme S1, Tables S1–S8, and Figures S1–S4). The protocol for the validation and optimization of the few parameters with high penalties was the same as CGenFF using the FFTK plugin tool of VMD as an input generator and refinement tool. The target data were generated with several quantum ab initio methods in Gaussian16 [33]. The penalty score returned for every bonded parameter and charge was used to guide the selective optimization of the charges and some dihedral angles; bonds, angles, and improper force constants did not require any optimization. The same equilibration protocol was used for all the simulations (see Supplementary Materials for details). The analysis was performed using in-house python scripts and the pyemma (http://emma-project.org/latest/, accessed on 5 March 2022) and mdtraj (https://www.mdtraj.org/, accessed on 5 March 2022) analysis tools.

### *2.2. Chemistry and Characterization*

#### 2.2.1. General

All chemical reagents were supplied by Sigma-Aldrich. Gibco (Thermo Fisher Scientific, Waltham, MA, USA) was the supplier for the biological products including fetal bovine serum (FBS), trypsin-EDTA, Dulbecco's modified Eagle's medium (DMEM), 1% penicillin/streptomycin, and L-glutamine. Unlabeled HA (50 KDa) and HA-FITC (50 KDa) were purchased from HAworks LLC. Anti-CD44-FITC and CD44 monoclonal antibodies (MA5-15462, 8E2F3) were purchased from Miltenyi Biotec and Invitrogen, respectively.

An Eppendorf Thermomixer® agitator (Eppendorf, Hamburg, Germany) was used for conjugations, while centrifugations were performed in an Eppendorf centrifuge. Analytical TLC was performed using Merck Kieselgel 60 $F_{254}$ aluminum plates and visualized by UV light. Evaporation was carried out in vacuo in a Büchi rotary evaporator, and the pressure controlled by a Vacuubrand CVCII apparatus. Purifications were carried out by flash column chromatography using silica gel (230–440 mesh ASTM, Merck KGaA, Darmstadt, Germany).

Nuclear magnetic resonance (NMR) spectra were recorded on a 400 MHz $^1$H and 101 MHz $^{13}$C NMR with a Varian Direct Drive spectrometer at room temperature. Chemical shifts (δ) are reported in parts per million (ppm) relative to the residual solvent peak. The multiplicity of each signal is given as s (singlet), d (doublet), t (triplet), and m (multiplet). *J* values are given in Hz. High-Resolution Electrospray Ionization (ESI-TOF) mass spectra were carried out on a Waters LCT Premier Mass Spectrometer.

2.2.2. Synthesis of 4-(3,4-Dihydroisoquinolin-2(1*H*)-yl)butan-2-one (**JE22**)

Compound **JE22** was synthesized as previously reported (Scheme 1), and the spectroscopic data are in agreement with those reported in the literature [34]. See Supplementary Materials for details.

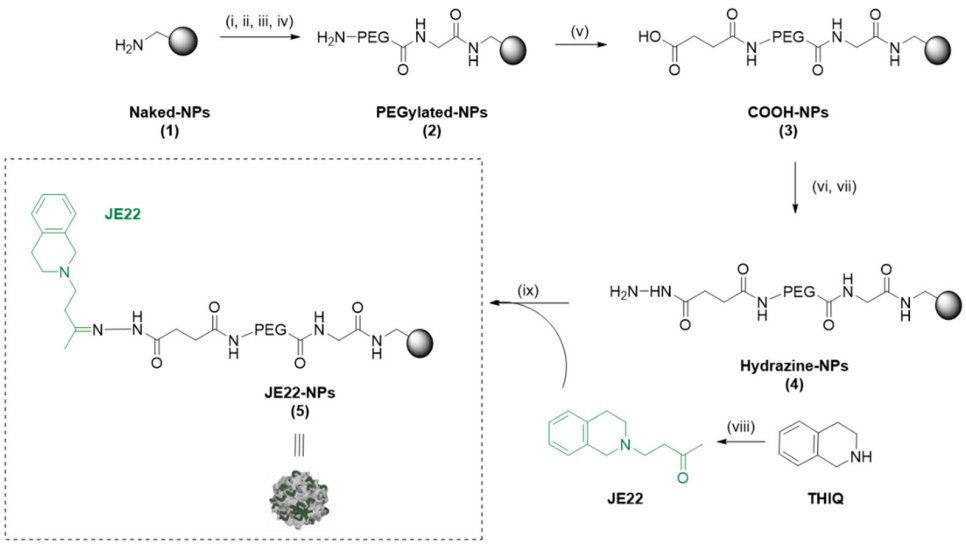


**Scheme 1.** General scheme of preparation of **JE22-NPs** (**5**)**.** Reagents and conditions. (i) Fmoc Gly-OH (50 eq.), Oxyme (50 eq.), DIC (50 eq.), DMF, 2 h, 60 °C; (ii) 20% Piperidine/DMF, 3 × 20 min, 25 °C; (iii) Fmoc-PEG-OH (50 eq.), Oxyme (50 eq.), DIC (50 eq.), DMF, 2 h, 60 °C; (iv) 20% Piperidine/DMF, 3 × 20 min, 25 °C; (v) Succinic anhydride (50 eq.), DIPEA (50 eq.), DMF, 2h, 60 °C; (vi) Oxyme (50 eq.), DIC (50 eq.), DMF, 4 h, 25 °C; (vii) Hydrated hydrazine 55% *v*/*v* (75 eq.), DMF, 15 h, 25 °C; (viii) methyl vinyl ketone, CuBr, $CH_2Cl_2$, 0 °C, 30 min then, 64 h rt.; (ix) **JE22** (10 eq.), TFA, MeOH, 15 h, 25 °C.

2.2.3. Preparation of Therapeutic Polymeric Nanoparticles **JE22-NPs** (**5**)

The synthesis of the polymeric nanoparticles **JE22-NPs** (**5**) is displayed in Scheme 1. Aminomethyl NPs (**Naked-NPs**, **1**) (1 mL, 3% SC, 64 µmol/g, 1 µmol, 1 eq.) were synthesized as previously reported (see Supplementary Materials for synthetic details) [17]. Then, **Naked-NPs** (**1**) were conditioned in *N*,*N*-dimethylformamide (DMF) (1 mL × 3 times). N-α-Fmoc-glycine (Fmoc-Gly-OH) (50 eq.) was mixed in DMF (1 mL) with oxyme (50 eq.) and *N*,*N*′-diisopropylcarbodiimide (DIC) (50 eq.) for 10 min at 25 °C. Then, this solution was added to **Naked-NPs** (**1**) and stirred for 2 h at 60 °C at 1400 rpm on the Thermomixer. Subsequently, the NPs were washed by centrifugation (13,400 rpm, 3–10 min) with DMF, MeOH, and water to obtain Fmoc-Gly-NPs (100% yield, 0.064 mmol $g^{-1}$ of amino groups). Then, Fmoc deprotection with 20% piperidine/DMF (3 × 20 min) was carried out. Separately, Fmoc-4,7,10-trioxa-1,13-tridecanediamine succinamic acid (Fmoc-PEG-COOH) spacer (50 eq.) was dissolved in DMF (1 mL), then oxyme (50 eq.) and DIC (50 eq.) were added and mixed for 10 min at 25 °C, and this last solution was mixed to NPs for 2 h at 60 °C. Subsequently, Fmoc deprotection was carried out to give **PEGylated-NPs** (**2**). Next, a solution of succinic anhydride (50 eq.) and *N*,*N*-diisopropylethylamine (DIPEA) (50 eq.) in DMF (1 mL) was added to NPs, sonicated, and mixed for 2 h at 60 °C. Next, **COOH-NPs** (**3**) were activated with oxyme (50 eq.) and DIC (50 eq.) for 4 h at 25 °C. NPs were centrifuged, and a solution of 55% *v*/*v* hydrazine hydrate (75 eq.) in DMF (1 mL) was added, and NPs were left stirring at 25 °C for 15 h. Subsequently, **hydrazine-NPs** (**4**) were washed and conditioned in MeOH. Finally, **JE22** (10 eq.) was dissolved in MeOH (1 mL) and added to NPs with a drop of trifluoroacetic acid (TFA), and the resulting mixture was stirred at 25 °C for 15 h on the Thermomixer at 1400 rpm. **JE22-NPs** (**5**) were afforded by centrifugation and subsequently washed with DMF (3 × 1 mL), MeOH (3 × 1 mL), and sterile ultrapure water (3 × 1 mL) (Scheme 1 and Table S9).

2.2.4. Characterization of **JE22-NPs** (**5**)

Particle size distribution and mean size were measured using dynamic light scattering (DLS) with biological grade water in a disposable cuvette. Zeta potential values were determined on a Zetasizer Nano ZS ZEN 3500 (NanoMalvern Panalytical, UK) using a transparent cuvette. NPs morphology and shape were analyzed by transmission electron microscopy (TEM) using a LIBRA 120 PLUS TEM (Carl Zeiss NTS GmbH, Oberkochen, Germany) and analyzed with Xei data acquisition software.

2.2.5. Stability Study of **JE22-NPs** (**5**)

For the stability study, 10 µL of NPs were incubated for 24 h in ultrapure water (Milli-Q grade, $H_2O$ mq), DMEM, NaCl 10 mM, NaCl 154 mM, and PBS at pH = 7 at 4 °C and 37 °C. Then, NPs were centrifuged and prepared in biological grade water, and subsequently, the particle mean size and size distribution were determined by DLS and zeta potential analysis.

2.2.6. Determination of Conjugation Efficiency of **JE22-NPs** (**5**)

Calculation of **JE22** conjugation efficiency (CE; %) and loading capacity (LC) was carried out by measurement of the concentration of free **JE22** in the supernatant obtained after the centrifugation of NPs by UV spectroscopy at 254 nm. Previously, an absorbance study of **JE22** at different concentrations and a calibration curve with lineal ratio between **JE22** concentration and the optical density of the compound was performed (Figure S10A,B). Subsequently, **JE22** LC and CE were calculated based on formulas as follows:

$$LC = \frac{[JE22\ conjugated\ on\ nanoparticle\ surface]}{Number\ of\ NPs} \times N_A \quad (1)$$

where $N_A$ is Avogadro's number.

$$CE\ (\%) = \frac{[JE22\ conjugated\ on\ nanoparticle\ surface]}{\begin{array}{c}Loading\ of\ free\ amine\ groups\\ on\ nanoparticle\ surface\end{array}} \times 100 \quad (2)$$

2.2.7. Evaluation of Drug Release Profile of **JE22-NPs** (**5**)

To determine the efficiency of the hydrolysis of the hydrazone bond of the **JE22-NPs** (**5**), samples at acidic and neutral pH were prepared. First, 200 µL ($8.81 \times 10^8$ NPs/µL) of NPs were incubated in a PBS solution at pH = 5 and pH = 7 for 120 h in an incubator at 37 °C. Then, the supernatants were collected by centrifuging each sample at $t$ = 1.5, 3, 6, 24, 48, 72, 96, and 120 h, and they were analyzed through high-performance liquid chromatography (HPLC) (Agilent 1200 series HPLC system) with a C18 column from Waters CORTECS™ (2.1 mm × 100 mm, 1.6 µm) [21]. The detection of PDA eλ for **JE22** was established at 252 nm. The mobile phase of water (0.1% formic acid): acetonitrile was supplied at a flow rate of 0.4 mL/min: 0% B, T8: 95% B, T8.1: 0% B, analysis time 10 min. Using standard samples, a calibration curve of **JE22** was prepared (Figure S10C). The maximum identification was confirmed by the retention time (RT) of **JE22** at 1.55 min. Cumulative release of **JE22** was performed using the following equation:

$$Cumulative\ JE22\ Release\ (\%) = \frac{D_t}{D_T} \times 100 \quad (3)$$

where $D_T$ is the total concentration of **JE22**-loaded onto the **JE22-NPs** (**5**), and $D_t$ is the concentration of **JE22** released from **JE22-NPs** (**5**) at a given time $t$ [21].

*2.3. Biology*

2.3.1. General

A NuAire NU-4750E US AutoFlow incubator was used for cell culture. Cell-based experiments were carried out in a TELSTAR BIO II Class II A laminar flow cabinet. Flow

cytometry assays were performed on a FACSCanto II system (Becton Dickinson & Co., Franklin Lakes, NJ, USA) using the Flowjo® 10 software (Becton Dickinson & Co., Franklin Lakes, NJ, USA) for analysis. Transmission electron microscopy was performed on a LIBRA 120 PLUS Carl Zeiss SMT microscope. Cell viability was carried out using a GloMax-Multi Detection System to measure fluorescence. Wound healing images were acquired using an Olympus CKX53 microscope, and wound areas were measured using ImageJ® software (version 1.49b, Rasband, W.S., U. S. National Institutes of Health, Bethesda, MD, USA). Confocal microscopy images were obtained using a Zeiss LSM 710 confocal laser scanning microscope and ZEN 2012 program Blue Edition (Carl Zeiss NTS GmbH, Oberkochen, Germany) for image acquisition.

#### 2.3.2. Cell Culture

Human breast carcinoma MDA-MB-231 and MCF-7 cells and human embryonic kidney-derived non-cancerous cells HEK-293 (provided by the Cell Bank the Center of Scientific Instrumentation of the University of Granada) (obtained from American Type Culture Collection ATCC, Manassas, VA, USA) were cultured in DMEM with serum (10% FBS), L-glutamine (2 mM), and 1% penicillin/streptomycin and incubated in a tissue culture incubator at 37 °C, 5% $CO_2$ and 95% relative humidity. Cells were frequently tested negative for mycoplasma infection.

#### 2.3.3. Cell Viability Assays

**JE22** was dissolved in DMSO and stored at −20 °C. For each experiment, the stock solution (100 mM) was further diluted in culture media to obtain the desired concentrations. MDA-MB-231 cells were seeded in a 96-well plate format (1000 cells/well) and incubated for 24 h before treatment. Each well was then replaced with fresh media, containing **JE22** (0.01–100 μM) and incubated for 5 days. Untreated cells (DMSO, 0.1% $v/v$) were used as control to detect any undesirable effects of culture conditions on cell viability. Each condition was performed in triplicates. PrestoBlue™ cell viability reagent (10% $v/v$) was added to each well and the plate incubated for 120 min. Fluorescence emission was detected using a GloMax-Multi Detection System (excitation filter at 540 nm and emission filter at 590 nm). All conditions were normalized to the untreated cells (100%) and the curve fitted using GraphPad Prism using a sigmoidal variable slope curve. The $EC_{50}$ (half-maximal effective concentration) value is expressed as the mean ± SD of three independent experiments.

For viability assays of **JE22-NPs** (**5**), MDA-MB-231 and HEK-293 cells were plated at 1000 cells/well (doubling times are 26 h and 24 h, respectively) and MCF-7 cells were plated at 2000 cells/well (doubling time is 34 h). After 24h, cells were nanofected with different ratios of **JE22-NPs** (**5**) (40,000, 20,000, 10,000, 5000, 2500, 1250, and 625 NPs/cell). Untreated cells, cells incubated with **Naked-NPs** (**1**) (40,000 NPs/cell), and NPs in culture medium in the absence of cells were used as controls. Each condition was performed in triplicate. Cell viability was tested at day 5 using PrestoBlue™ reagent and curve fitted as previously described. For viability assays of **JE22-NPs** (**5**) at acidic conditions, cells were treated with 40,000 NPs/cell in DMEM media at pH = 5. DMEM media at pH = 5 were prepared by replacing sodium bicarbonate with PIPES buffer (10 mM) and adjusting the pH with NaOH. Untreated cells, cells incubated with **Naked-NPs** (**1**) (40,000 NPs/cell), and NPs in culture medium in the absence of cells were used as control. After 1.5 h of incubation, media were replaced with pH = 7.4 DMEM media and cell viability was tested at day 5 as described above. Each condition was performed in triplicates.

#### 2.3.4. Confocal Microscopy Analysis

Glass coverslips were coated with poly-L-lysine ($10 \times 10^4$ cells/well), and then MDA-MB-231 cells were seeded onto them in 24-well plate format. Following incubation time (24 h), cells were stained using an anti-CD44-FITC antibody diluted in MACS® BSA Stock Solution (1 μL/400 μL, Miltenyi Biomedicine GmbH, Bergisch Gladbach, Germany). Plates

were incubated for 10 min on ice in the dark. Then, cells were washed with DMEM media and treated with a new solution of culture media containing **JE22-NPs** (**5**) fluorescently labeled with Cy5 (1000 NPs/cell). After 30 min of incubation at 37 °C, the medium was aspirated, and the cells were washed twice with 1 × PBS and fixed in 4% paraformaldehyde for 10 min at room temperature. After washing with 1 × PBS, fixed cells were mounted with DAPI-containing mounting medium (ProLong Gold, Life technologies, Renfrew, UK). A ZEISS LSM 710 confocal laser microscope (Carl Zeiss NTS GmbH, Oberkochen, Germany) was used to collect the images using a DIC Plan-Apochromat 63× oil immersion objective with 1.40 numerical apertures and the ZEN 2010 software (Carl Zeiss NTS GmbH, Oberkochen, Germany). Images were subsequently analyzed with both the Zen 2012 Blue Edition Image and ImageJ softwares (version 1.49b, Rasband, W.S., U. S. National Institutes of Health, Bethesda, MD, USA).

#### 2.3.5. HA-FITC Binding Assay

Adherent MDA-MB-231 cells were trypsinized, counted, and diluted in DMEM in order to have $5 \times 10^4$ cells/eppendorf tube. Cells were centrifuged for 5 min, and pellets were resuspended in DMEM media containing **JE22-NPs** (**5**) (40,000 NPs/cell) or **JE22** in solution (120 μg/mL). Anti-CD44 antibody was used as control (120 μg/mL). Samples were incubated at 4 °C for 30 min. Then, cells were centrifuged for 5 min, and pellets were resuspended in DMEM media containing HA-FITC (20 μg/mL) and incubated at 4 °C for 15 min. Cells incubated with unlabeled HA were used as the negative control, whereas cells incubated with HA–FITC served as the positive control. After incubation, cells were centrifuged and resuspended in PBS, and samples were analyzed by flow cytometry (FACSCanto II, Becton Dickinson & Co., Franklin Lakes, NJ, USA). Flowjo® 10 software (Becton Dickinson & Co., Franklin Lakes, NJ, USA) was used for data analysis. Results are expressed as the fluorescence intensity mean ± SD of three independent experiments.

#### 2.3.6. Wound Healing Assay

MDA-MB-231 cells were seeded in a 12-well plate format at $25 \times 10^4$ cells/well and incubated until 90% confluence. Then, cells were gently scratched using a pipette tip, washed with PBS to remove cell debris, and treated with **JE22-NPs** (**5**) at 20,000 NPs/cell (36 nM) and **JE22** ($EC_{50}$ = 8 μM). Untreated cells (DMSO, 0.1% $v/v$) and cells treated with **Naked-NPs** (**1**) at 20,000 NPs were used as controls. Images were acquired at time zero and after 24 h of incubation using an Olympus CKX53 microscope (4× objective magnification). Wound areas were measured using ImageJ® software (Rasband, W.S., U. S. National Institutes of Health, Bethesda, MD, USA).

#### 2.3.7. Apoptosis Assay

MDA-MB-231 and MCF-7 cells were seeded at $5 \times 10^4$ cells/well in a 24-well plate. After 24 h, cells were treated with **JE22-NPs** (**5**) at 20,000 NPs/cell (36 nM), **JE22** ($EC_{50}$ = 8 μM and 4 × $EC_{50}$ = 32 μM), and **Naked-NPs** (**1**) (20,000 NPs/cell) for 24 h. Cells incubated in the absence of the apoptosis inducing agent were used as the negative control, whereas cells incubated with $H_2O_2$ (2 mM) for 4 h at 37 °C served as the positive control. The experiments were performed using the Annexin V-FITC detection kit (Tali Apoptosis Kit -Annexin V Alexa Fluor 488 and propidium iodide (A10788, Invitrogen Europe Limited, Renfrew, UK)) according to the manufacturer's instructions, and the samples were analyzed by flow cytometry with a FACSCanto II flow cytometer. Flowjo® 10 software was used for data treatment. The analysis was performed in three independent assays.

#### 2.3.8. Statistical Analysis

A one-way analysis of variance (ANOVA) was performed using Sigmastat 3.5 statistical analysis software.

## 3. Results and Discussion

### *3.1. Study of the Effect of Structural Modification of THIQ on CD44 Interaction by Computational Studies*

To assess whether the functionalization with ketone does not affect the interaction with the CD44, a computational study was performed. For this purpose, the protein–ligand interactions between the murine CD44 HABD and **JE22** at an atomist level were analyzed. MD simulations using the crystallized CD44 HABD with **THIQ-ester** derivative were performed using the same protocols after substituting one residue by the other (Figure 2A,B). A typical setup of the MD simulations with an explicit solvent is shown in Figure 2A for the protein with one of the ligands.

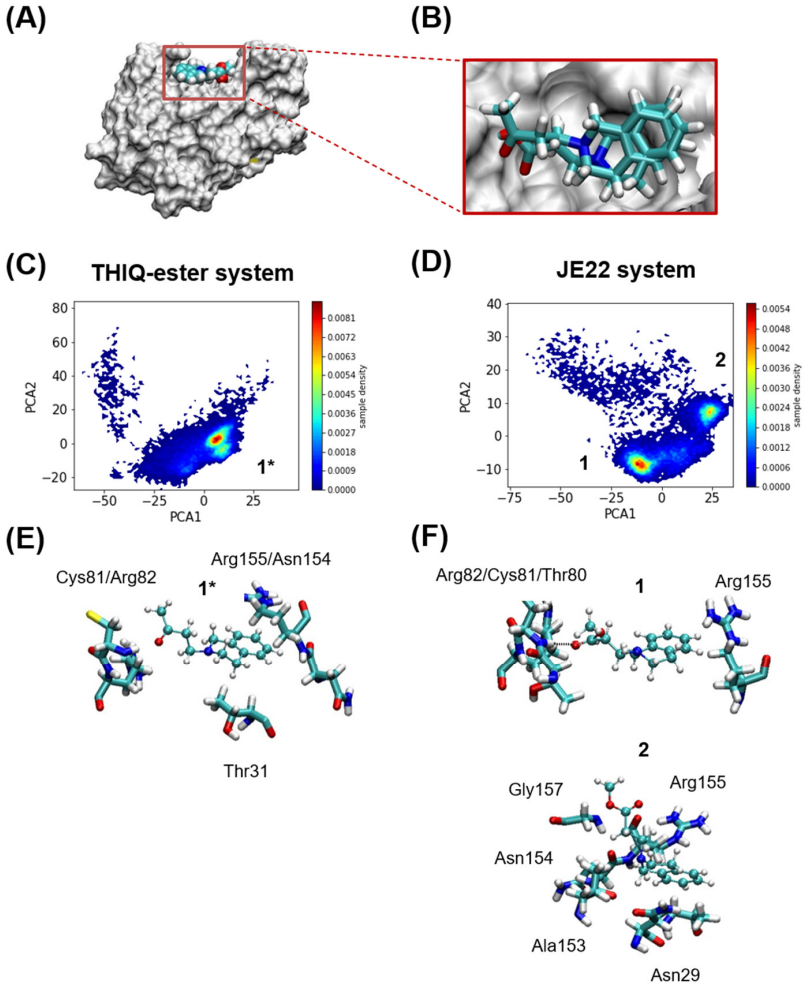


**Figure 2.** Computational analysis. (**A**) Murine CD44 HABD in MSMS representation in white, and **THIQ-Ester** in VDW representation at the position where it is found in the crystal structure PDB id 5BZK, used as starting point of the MD simulations. (**B**) Relative positions of **JE22** and **THIQ-ester** ligands at the start of the MD simulations. The **JE22** molecule was aligned using the position of the **THIQ-ester** ligand in the crystal structure PDB id 5BZK. (**C**,**D**) Comparison of MD-resolved ligand binding poses (**1*** for **THIQ-ester** system and **1** and **2** for the **JE22** system). Probability density of the first two principal of the multidimensional matrix built with the distances between either the nitrogen and oxygen atoms of (**C**) **THIQ-ester** or (**D**) **JE22**, and any of the nitrogen or oxygen atoms of the residues that define the **THIQ-ester** binding pocket. The binding pocket where **THIQ-ester** is found crystallographically is formed by residues Asn29, Thr31, Glu41, Thr80, Cys81, Arg82, and Arg155; any of these residues have at least one atom at 3 Å of the ligand. (**E**,**F**) Representative structures of each cluster are shown in panels (**E**,**F**) for **THIQ-ester** and **JE22** systems, respectively. The residues from the protein where there is at least an atom within 2.5 Å of the ligand are shown in licorice representation.

In order to further characterize the multiple poses that we observed in the MD trajectories of either ligand, we next performed a cluster analysis using principal component analysis (PCA) and the distances between (i) the center of mass of the N and O atoms of **JE22** or **THIQ-ester** and (ii) the center of mass of N and O atoms of residues Asn29, Thr31, Thr80, Cys81, Arg82, and Arg155. These residues are those that have at least one atom within 3 Å from the ligand at the beginning of the simulation. The data were filtered, and only when the minimum distance between the protein residues and either **JE22** or **THIQ-ester** was less than 3 Å, they were kept. Subsequently, a PCA was performed over the resulting multidimensional matrix of distances. 95% of the variance of the data was explained with the sum of the eight first principal components (PCs) (Figure 2C,D). Clustering was just performed with only the first two PCs that amounted to ~70% of the variance. This analysis was performed with a Kmeans algorithm using four clusters as initial guess; two of the clusters were rather localized and the others two were disperse (Figure 2E,F).

These computational studies have demonstrated that **JE22** binds to murine CD44 HABD in an almost identical fashion than **THIQ-ester** derivative, which is found in the reported crystallographic structure [16]. Based on these results, we can confirm that the designed THIQ ketone derivative **JE22** is a good candidate to interact with CD44 receptor.

### *3.2. Synthesis and Physicochemical Characterization of the Nanodevice to Target CD44*

#### 3.2.1. Preparation of **JE22-NPs** (**5**)

Following a previously described protocol, a monodisperse population of amino-functionalized polystyrene nanoparticles cross-linked with divinylbenzene were synthesized by dispersion polymerization, using vinyl benzyl amine hydrochloride—VBAH—as the monomer to functionalize the nanoparticle with the amino groups [17]. Following an Fmoc solid-phase protocol, **Naked-NPs** (**1**) (0.064 mmol $g^{-1}$ of amino groups) were PEGylated to obtained **PEGylated-NPs** (**2**) (100% yield). The PEGylation increases the biocompatibility of the NPs and reduces unfavorable interactions between NPs and the bioactive cargoes. The modified THIQ derivative of CD44 inhibitor (**JE22**) was synthesized as described in Scheme 1. Ketone moiety to allow for conjugation to the nanoparticle by hydrazine formation was achieved by the Michael addition of THIQ to methyl vinyl ketone, employing cupper bromide (I) as a catalyst (Scheme 1). The structure of the obtained compound **JE22** was confirmed by NMR and mass spectra (Figures S5 and S6). Then, drug loading was carried out by conjugation of the CD44 inhibitor **JE22** via hydrazone bond [20]. For this purpose, carboxylated nanoparticles **COOH-NPs** (**3**) were prepared using succinic anhydride; then, **hydrazine-NPs** (**4**) were prepared by treatment with hydrazine, and the selective conjugation to the ketone group of THIQ derivative **JE22** was carried out to yield **JE22–NPs** (**5**) (Scheme 1).

#### 3.2.2. Physicochemical Characterization of **JE22-NPs** (**5**)

The size distribution of the nanoparticles loaded with THIQ ketone derivative **JE22-NPs** (**5**) and **Naked-NPs** (**1**) were measured by DLS (Figure 3A). A monodisperse population was observed with a hydrodynamic diameter of 382.5 ±0.9 nm (PDI = 0.13) (Figure 3A). TEM analysis revealed the spherical shape of these nanoparticles and corroborated their size (Figure 3D). The zeta potential of **JE22-NPs** (**5**) and **Naked-NPs** (**1**) was also determined. The value for the new nanoformulation was slightly negative (−24.1 mV ± 0.7) in water (Figure 3B).

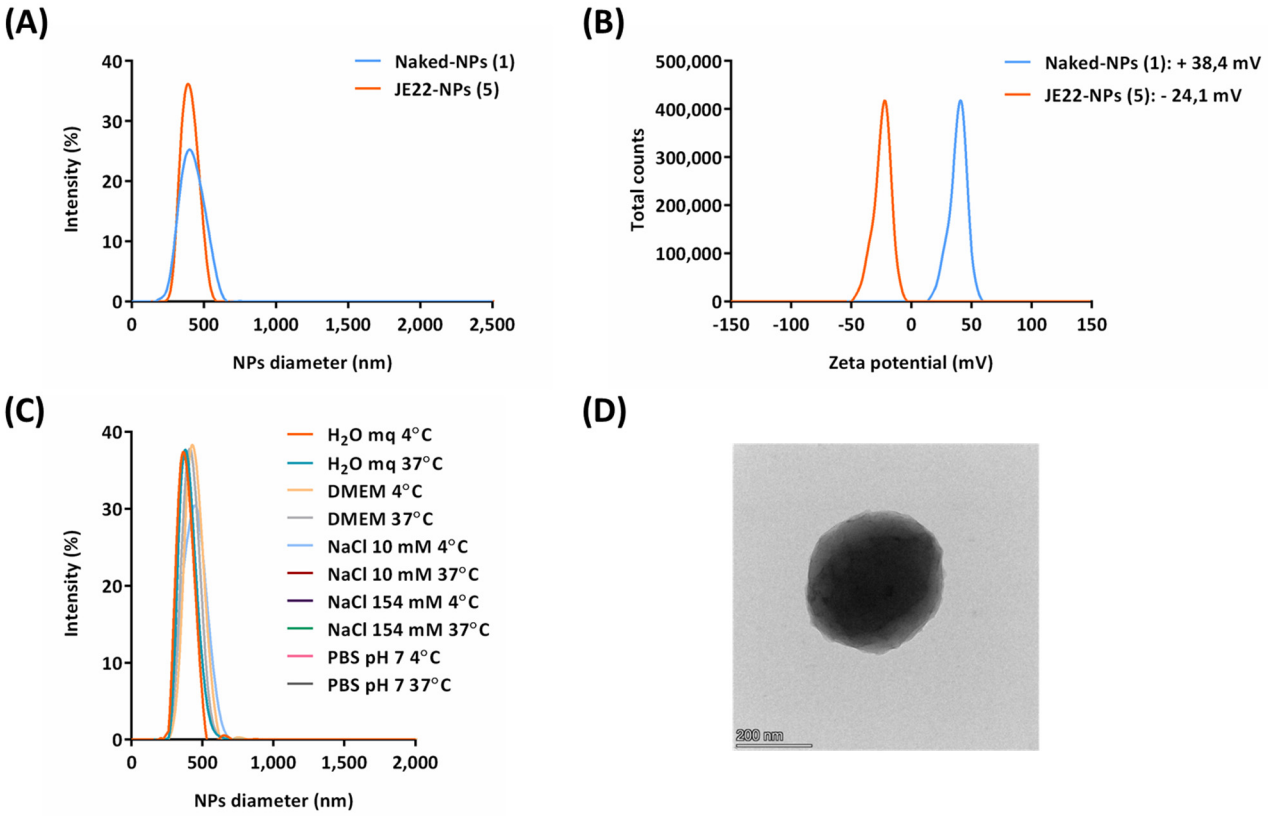


**Figure 3.** Characterization of **JE22-NPs** (**5**). (**A**) Hydrodynamic diameter values by DLS. (**B**) Zeta potential values. (**C**) DLS analysis of stability of **JE22-NPs** (**5**) for 24 h at 4 °C and 37 °C in sterile ultrapure $H_2O$ mq, DMEM, NaCl 10 mM, NaCl 154 mM, and PBS pH = 7. (**D**) Image of **JE22-NPs** (**5**) obtained by TEM.

Next, the stability of **JE22-NPs** (**5**) was evaluated in different conditions at 4 °C and 37 °C following guidelines provided by the European Nanomedicine Characterization lab. The size of these nanodevices was measured by DLS after 24 h in several sterile media: ultrapure water (Milli-Q grade, $H_2O$ mq), DMEM, NaCl 10 mM, NaCl 154 mM, and PBS pH = 7, showing a constant size distribution (Figure 3C). It was observed that neither the temperature nor the composition of the vehicle affected the stability of these nanoparticles. These results were corroborated by the zeta potential analysis (Figure S9). Overall, the stability of these particles was confirmed, which is a key point for future translation of this nanodevice.

### 3.2.3. Efficiency of Conjugation and Drug Release of **JE22-NPs** (**5**)

The quantification of the remaining amount of drug in the supernatant of the reaction can give information about the efficiency of the conjugation of anti-CD44 derivative **JE22** to the nanoparticles. For this purpose, a calibration curve of **JE22** was generated measuring a set of standard samples by UV spectroscopy ($A_{254}$ nm) (Figure S10). Then, the LC value was determined by considering the amount of conjugated **JE22** with respect to the number of nanoparticles, and this approach is more accurate than nanoparticle weight [35]. To this aim, the number of nanoparticles per volume was determined using an accurate spectrophotometric method that was previously developed [36]. The concentration of nanoparticles **JE22-NPs** (**5**) was estimated as $4.8 \times 10^6$ NPs/mL (Figure S7). The drug LC is related to the number of nanoparticles; thereafter, the LC per nanoparticle can be calculated. A LC of $1.14 \times 10^7$ molecules of **JE22** per nanoparticle was estimated. This value corresponds to $1.89 \times 10^{-8}$ nmol of CD44 inhibitor **JE22** per NP (Figure 4A).

**(A)**

| Nanoparticles | JE22 loading | |
|---|---|---|
| | C.E. (%) | L.C. (Molec./NP) |
| JE22-NPs (5) | 100 | $1.14\times10^{7}$ |

**C.E.** = Conjugation efficiency; **L.C.** = Loading capacity; **Molec.** = Molecules

**(B)**

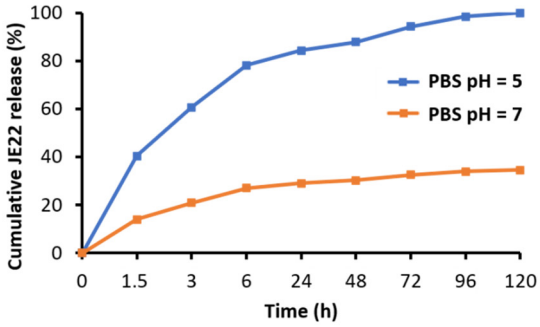


**Figure 4.** Evaluation of drug loading and release from **JE22-NPs** (**5**). (**A**) Determination of CE and LC of **JE22** per nanoparticle. (**B**) Cumulative **JE22** release. **JE22-NPs** (**5**) were incubated for 120 h in PBS at pH = 5 and pH = 7 at 37 °C. Results are expressed with the values of the mean ± SEM.

To determine the value of drug dose with accuracy and precision is of extreme relevance for the clinical translation of nanomedicine. The CE was determined by considering the drug conjugated with respect to the total amount of free amine groups on the nanoparticle surface, which was 100% for **JE22-NPs** (**5**) (Figure 4A). This high efficiency is remarkable compared to drug-loading strategy based on encapsulation [37].

To achieve selective release at the target site, a pH-sensitive stimuli discharge strategy was implemented. Based on the fact that there is slightly acidic pH at the tumor microenvironment, a cleavable bond that responds to acidic pH was implemented [38]. To release the drug in acidic conditions, **JE22** was covalently conjugated to nanoparticles by a hydrazone bond sensitive to pH = 5–6 as previously reported [35]. The pH-responsive release of THIQ derivative **JE22** in vitro was determined by HPLC. A comparison of the percentage of the released drug with respect to the amount of CD44 inhibitor conjugated to the **JE22-NPs** (**5**) was done. Release profiles were obtained for five days at pH = 5 and pH = 7.4 by HPLC analysis (Figure 4B). As expected, the pH-sensitive cleavage of the hydrazone linker resulted in the exponential sustained release of **JE22** in an acidic environment (pH = 5 PBS) (Figure 4B, blue line). An accumulative release was achieved for up to 5 days (120 h). A significant release was observed within 6 h of incubation at pH = 5 with a release rate of 78% ± 0.6. Then, the maximum release value of 100% was achieved by a sustained release for up to 120 h. Non-significant size change was observed following incubation at pH = 5 for this period (see Figure S8). On the other hand, the amount of drug released from the nanodevice was minimal at physiological environment (pH = 7.4 PBS), (~20% within 6 h of incubation). This result demonstrates that a significant amount of the drug remained attached to the nanoparticles (Figure 4B, orange line). This result pointed out the realistic stability and selectivity of the **JE22-NPs** (**5**). It is important to remark that the pH value of the medium has a clear effect on the release efficiency of the drug, which validates the drug release strategy designed in this approach. Then, the efficient release of the drug in a sustained manner in acidic conditions could be a key feature to improve the therapeutic efficacy of **JE22-NPs** (**5**) in the tumor site.

### *3.3. Evaluation of Efficiency of the Designed Nanodevice **JE22-NP** (**5**) for Antitumor Activity*

Assessment of Biological Activity of **JE22-NPs** (**5**)

In order to assess the biological activity of this nanodevice to target CD44, in agreement with previous studies [39,40], two breast cancer cell lines expressing different levels of CD44 were selected: MDA-MB-231 with a high level and MCF-7 with a low level of CD44 expression, respectively. Analysis of CD44 expression by flow cytometry using an anti-CD44 antibody labeled with fluorescein (anti-CD44-FITC) confirms the suitability of these cell lines for testing CD44 inhibition (Figure S11).

The half maximal efficacy concentration ($EC_{50}$) of this therapeutic nanodevice **JE22-NPs** (**5**) in MDA-MB-231 cells was determined. For this purpose, cell viability was moni-

tored using fluorescent resazurin assay. $EC_{50}$ values were calculated from the generated 10-point semilog dose–response curves (Figure 5A–C). Initially, MDA-MB-231 cells were treated for 120 h with increasing concentrations of **JE22** in solution (0.001 to 100 μM) to determine the range of doses of inhibitor required to achieve the antiproliferative activity. Free **JE22** has an $EC_{50}$ value of 8 μM in MDA-MB-231 cells (Figure 5A). Then, a range of different concentrations of **JE22-NPs** (**5**) (312–40,000 NPs/cells, that corresponds to 0.6–72 nM) were incubated for 120 h with MDA-MB-231 cells. The $EC_{50}$ value for therapeutic NPs (**JE22-NPs, 5**) was calculated to be 49 nM (Figure 5C), which corresponds to 27,367 NPs/cell (Figure S14). This value indicated that the nanosystem offers a 150-fold reduction of the amount of **JE22** required to have the same effect than the free form has in tumor cells overexpressing CD44. In addition, treatment of CD44 low-expression MCF-7 cells with **JE22-NPs** (**5**) show no significant reduction of cell viability (Figure S12), reinforcing the selective effect of the nanodevice against CD44.

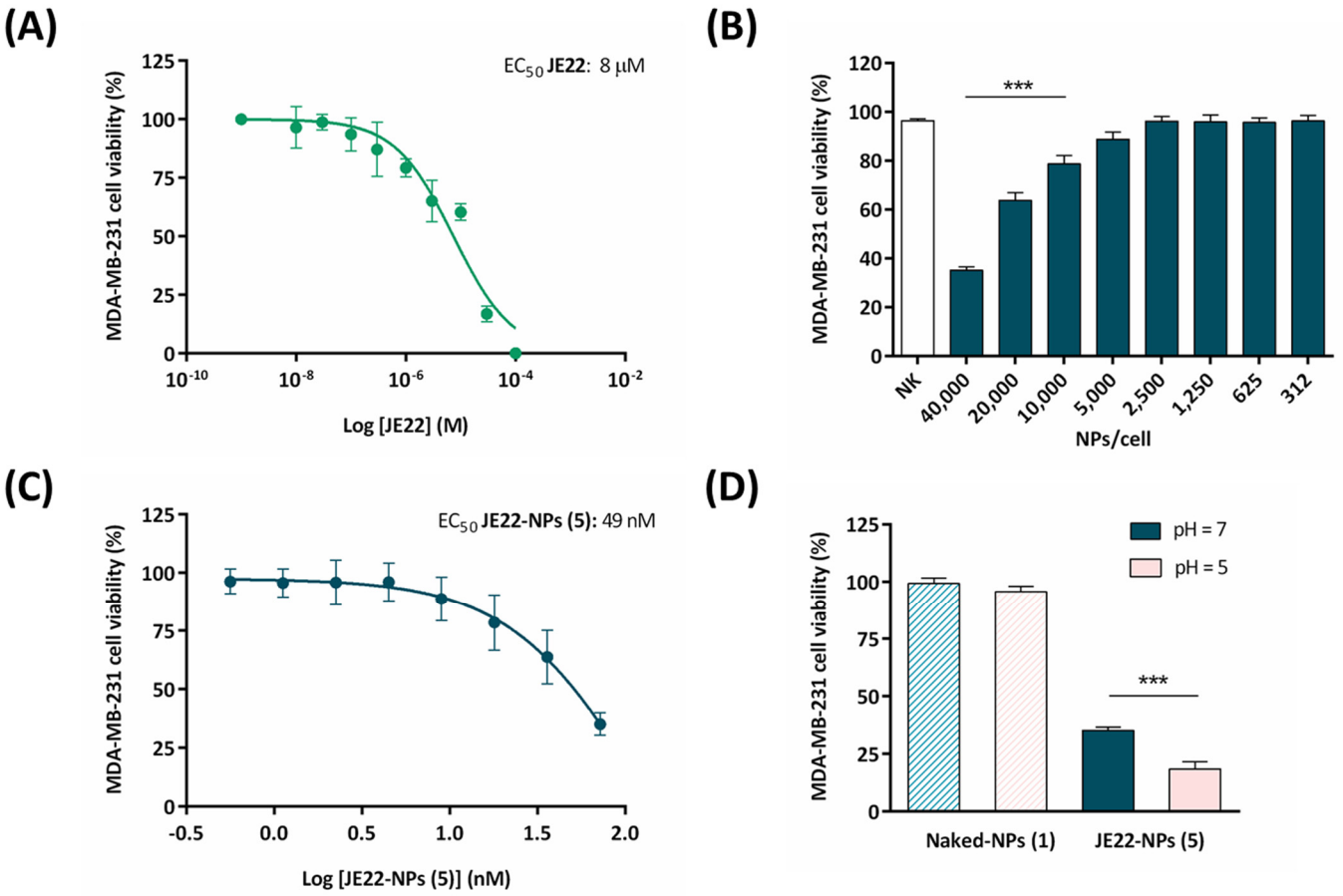


**Figure 5.** Evaluation of cell viability of the designed nanodevice (**JE22-NP, 5**) (**A**) Dose–response curves for **JE22** against MDA-MB-231 cells after 5 days of treatment. Error bars: ±SD from $n = 3$. (**B**) Bar graph showing the effect of **JE22-NPs** (**5**) on cell viability of MDA-MB-231 cell line. A standard range of added nanoparticles per cell (NPs/cell) to evaluate cell viability was used (from 312 to 40,000). Calculation of the NPs/cell was based on the number of NPs per volume (Figure S7). **Naked-NPs** (**1**) (NK) were used as control. Data represent the mean ± SD of three independent experiments; *** $p < 0.001$ (ANOVA). (**C**) Dose–response curve (percentage of cell viability versus concentration) of MDA-MB-231 cells after treatment with **JE22-NPs** (**5**), represented in molarity (nM). $EC_{50}$ value was obtained by the logarithm versus normalized response: variable slope using the GraphPad software. (**D**) Therapeutic effect representation by bar graph of **JE22-NPs** (**5**) at pH = 7.4 versus cell viability at pH = 5. Cell viability was tested after 5 days. **Naked-NPs** (**1**) were used as control. The experiments were carried out in triplicate, and the results are expressed with the values of the mean ± SD; *** $p < 0.001$ (ANOVA).

To further verify the selectivity of the nanodevice targeting the CD44 receptor in the MDA-MB-231 cancer cell line, we performed a competitive binding experiment. Cells were preincubated with the anti-CD44 antibody before treatment with **JE22-NPs** (**5**), showing a significant decrease of the antiproliferative effect respect to cells without pretreatment (Figure S13). These results showed that pretreating cells with the antibody effectively blocked CD44 cell-binding sites, preventing the recognition of epitopes from the nanodevices, showing that therapeutic effect of **JE22-NPs** (**5**) is linked to CD44 recognition.

Based on the fact that tumor tissues are characterized by an acidic extracellular pH as a result of the altered cancer cell metabolism compared to normal tissues, we applied a chemical strategy to achieve the release of the drug from the nanodevice in acidic conditions. To mimic the acidic tumor microenvironment, we used bicarbonate-free DMEM buffered with 10 mM of PIPES to fix a slightly more acidic external medium. We first tested whether cell viability could be affected after the incubation of MDA-MB-231 cells with pH = 5 DMEM media. After 1.5 h of incubation, no signs of cell death were observed, although a significant reduction of cell viability was obtained after 3 and 6 h of incubation (Figure S15). In order to test the effect of this selective release in the antiproliferative effect, we performed a comparative experiment incubating the cells in standard conditions (DMEM medium, pH = 7.5) and in the presence of DMEM buffered with PIPES to guarantee a slightly more acidic external medium (pH = 5). The results indicate that cytotoxic activities have pH dependence. Remarkably, **JE22-NPs** (**5**) showed to be more cytotoxic at acidic extracellular pH = 5 following only 1.5 h of incubation compared to under conventional conditions (pH = 7.4) for 5 days (see Figure 5D). This result is in agreement with the maximum peak of release of compound by HPLC analysis. A sustained drug release under physiological conditions can occur due to the acidification of culture media overtime [41]. As expected, the pH does not have any significant effect in cell viability when cells are treated with **Naked-NPs** (**1**)**.** These results suggest that specific release in acidic conditions is crucial for the therapeutic activity of this compound.

Finally, the cytotoxic effect of this nanodevice for non-cancerous cells was evaluated. We have used the human embryonic kidney-derived non-cancerous cells (HEK-293) to analyze the cell viability of **JE22-NPs** (**5**). No sign of death was observed after treatment of the normal cells with the nanodevice (Figure S16).

Overall, the nanoparticles were toxic to CD44+ cells and non-toxic to CD44- and non-cancerous cells.

### *3.4. Evaluation of Efficiency of the Designed Nanodevice for the Inhibition of CD44 Receptor Binding*

#### 3.4.1. Analysis of the Interaction of the Designed Nanodevice **JE22-NPs (5)** with CD44+ Cells by Confocal Microscopy

A confocal microscopy approach was carried out to study the location of the nanoparticles loaded with **JE22** on the surface of the CD44+ cells. MDA-MB-231 cells were immunolabeled with a fluorescently tagged primary anti-CD44 antibody (anti-CD44-FITC) [42]. Then, cells were treated with **JE22-NPs** (**5**) labelled with a cyanine derivative (Cy5, excitation 651 nm and emission 670 nm) to track them by fluorescence microscopy (see protocol for fluorescent labelling in Supplementary Materials, Section S5). It can be observed that the extracellular location of the **JE22-NPs** (**5**) is on the cellular surface where CD44 receptor is expressed (Figures 6 and S17).

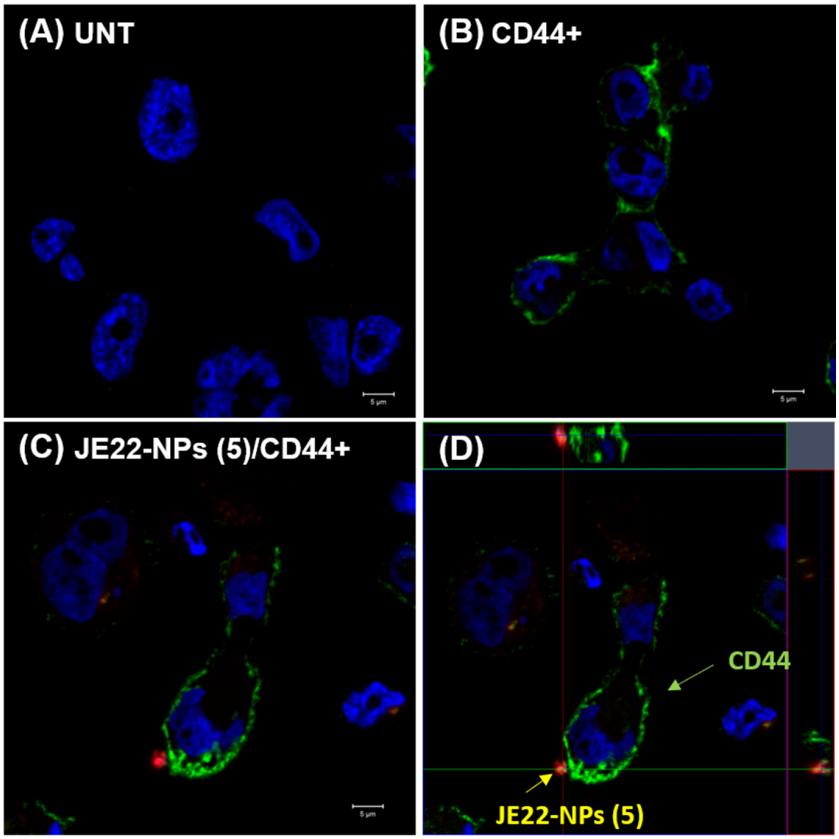


**Figure 6.** Confocal microscopy analysis of MDA-MB-231 (CD44+) cells treated with **JE22-NPs** (**5**). CD44-labeled cells treated with **JE22-NPs** (**5**) fluorescently labeled with Cy5 were analyzed (**C**) (Scale bar: 5 μm). The cells were incubated for 30 min with 1000 NPs/cell. Untreated cells (**A**) and cells labeled with anti-CD44-FITC (**B**) were used as controls (Scale bar: 5 μm). Images with an increase of 63× show a composition of the three channels used: blue, DAPI for the nucleus; green, FITC for anti-human CD44; and red, APC for **JE22-NPs** (**5**). (**D**) Confocal microscopy orthogonal (xy, xz, and yz) view representing the planes of intersection at the position of green cross line. The maximum intensity projection of the z-stack is shown blue for nuclei (DAPI), green for anti-human CD44 (FITC), and red for **JE22-NPs** (**5**) (APC).

#### 3.4.2. Assessment of CD44-Binding Capacity

To assess the CD44-binding capacity of the THIQ derivative **JE22** in solution and conjugated to the nanodevice, we performed a competitive binding assay using a fluorescent-labeled derivative of HA as natural ligand of CD44 (HA-FITC), which has high capacity of binding the CD44 receptor. For this purpose, we followed a previously reported method with slight modifications [43]. Briefly, cells overexpressing CD44, MDA-MB-231 cells, were pre-incubated with **JE22** and **JE22-NPs** (**5**) at 4 °C, and physiological pH for 30 min to allow for their binding to CD44 receptor on the cell surface. Then, cells were incubated with HA-FITC at 4 °C for 15 min, and fluorescence analyzed by flow cytometry. Anti-CD44 antibody was used as positive control. Cells incubated with unlabeled HA were used as negative control. As observed in Figure 7, pre-incubation with **JE22** displaced HA-FITC binding, yielding a statistically significant reduction of the fluorescence intensity (1.3-fold reduction) compared to the cells incubated with HA-FITC and cells pretreated with anti-CD44 monoclonal antibody (2.20-fold reduction). It is remarkably the fact that, as we expected, when cells were pretreated with the designed nanodevice **JE22-NPs** (**5**), no significant displacement was observed. This result reinforces our initial hypothesis that brought us to design a pH-sensitive strategy to release the CD44 inhibitor from the nanodevice at the acidic tumor microenvironment to enhance the efficient interaction with the CD44 receptor and to significantly reduce HA binding.

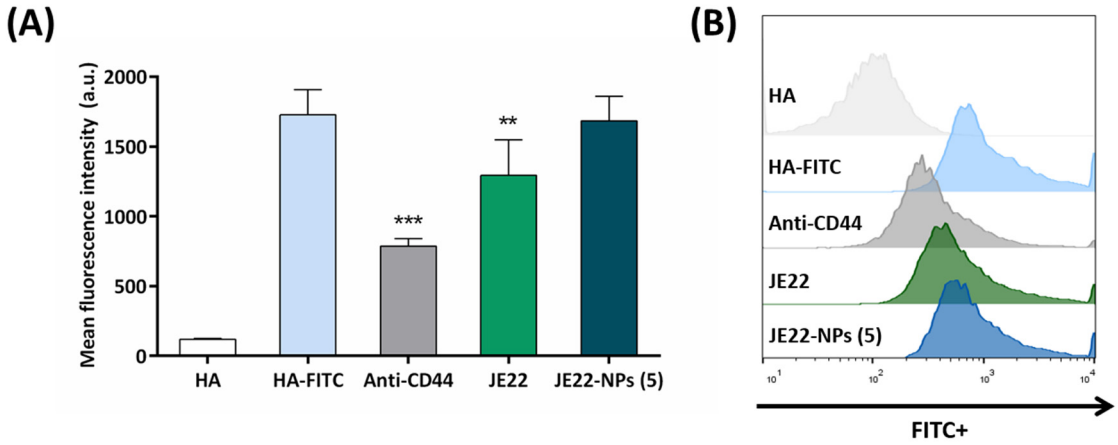


**Figure 7.** Inhibition of the HA–CD44 interaction by flow cytometry. (**A**) Mean fluorescence of MDA-MB-231 cells analyzed by flow cytometry after treatment for 30 min at 4 °C with **JE22-NPs** (**5**), **JE22,** and anti-CD44 followed by incubation with HA-FITC for 15 min at 4 °C. Cells treated with unlabeled HA and HA-FITC were used as the negative and positive control, respectively. Error bars: ±SD from $n = 3$; $p < 0.01$, **; $p < 0.001$, *** (ANOVA). (**B**) Flow cytometry overlay histograms of HA-FITC competitive assay binding to MDA-MB-231 cells.

### 3.4.3. Influence of **JE22-NPs** (**5**) in Migration of CD44+ Cells

Cell migration participates in numerous physiological and pathological processes. Previous studies have shown that CD44 proteins can stimulate tumor cell proliferation, motility, and invasion [44].

To detect whether this nanodevice can decrease the migration of CD44+ cells and, consequently, modify any mesenchymal behavior, a scratch-wound healing migration assay was performed to determine whether **JE22-NPs** (**5**) compared to free **JE22** could halt migration of MDA-MB-231 cells, as would be expected for a CD44 inhibitor [45]. After making the wound, MDA-MB-231 cells were treated with CD44 inhibitor **JE22** free and conjugated to nanodevice **JE22-NPs** (**5**) for 24 h and compared with untreated cells (0.1% $v/v$ DMSO) and cells treated with the nanodevice without drugs (**Naked-NPs, 1**), respectively. Cells treated with THIQ derivative **JE22** in solution significantly reduced cell motility; wound closure was reduced to 15.09 ± 4.90% compared with cells treated with DMSO (30.21 ± 6.06%). Remarkably, when MDA-MB-231 cells were treated with **JE22** conjugated to the nanodevice **JE22-NPs** (**5**), cell migration reduction was significantly higher than with **JE22** in solution (4.89 ± 2.77%) (Figure 8). The fact that the concentration used in this assay is lower than the $EC_{50}$ (20,000 NPs) (Figure 5B) suggests that the migration effect could be independent of the cytotoxic effect.

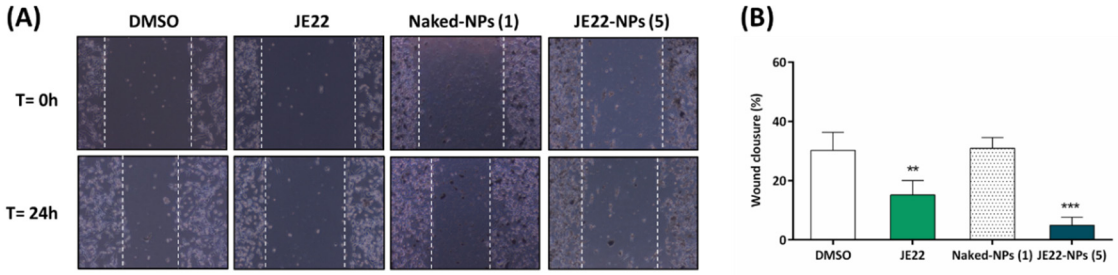


**Figure 8.** Scratch-wound migration assay. (**A**) Snapshots of the scratch-wound area of MDA-MB-231 cells treated with DMSO, **JE22**, **Naked-NPs** (**1**), and **JE22-NPS** (**5**) at time zero (top) and after 24 h (bottom). White lines highlight the gap created by the scratch. (**B**) Bar graph showing the percentage of wound closure of MDA-MB-231 cells after treatment with **JE22** and **JE22-NPs** (**5**) compared to untreated cell control (DMSO) and cells treated with **Naked-NPs** (**1**), respectively. Error bars: ±SD from $n = 3$; $p < 0.01$, **; $p < 0.001$, *** (ANOVA).

3.4.4. Apoptotic Activity of **JE22-NPs** (**5**)

To rule out that the observed delay in gap closure was caused by **JE22**-induced cell death, cell viability was examined by Annexin V/PI staining after treatment. Annexin V/PI staining is a widely used method to study apoptotic cells. Annexin V/PI significantly regulates the viable, necrotic, and apoptotic cells through differences in plasma membrane permeability and integrity [46]. We first study the apoptotic effect of **JE22** against CD44+ MDA-MB-231. Even at four times the $EC_{50}$ concentration of the drug, no crucial apoptotic effect was observed (Figure 9). These results suggest that apoptosis is not the mechanism by which **JE22** induces cell death. Then, the apoptotic effect of the **Naked-NPs** (**1**) and **JE22-NPs** (**5**) was analyzed to check that no apoptotic effect is caused by the nanocarrier itself. As expected the concentration of nanoparticles **JE22-NPs** (**5**) that we used in this assay (20,000 NPs) did not induce significant apoptosis or necrosis in either MDA-MB-321 cells (Figure 9) or MCF-7 (Figure S18). However, gap closure was inhibited at the same concentration (Figure 8). These results reinforce the fact that the migration effect could be independent of the cytotoxic effect of **JE22-NPs** (**5**) [47].

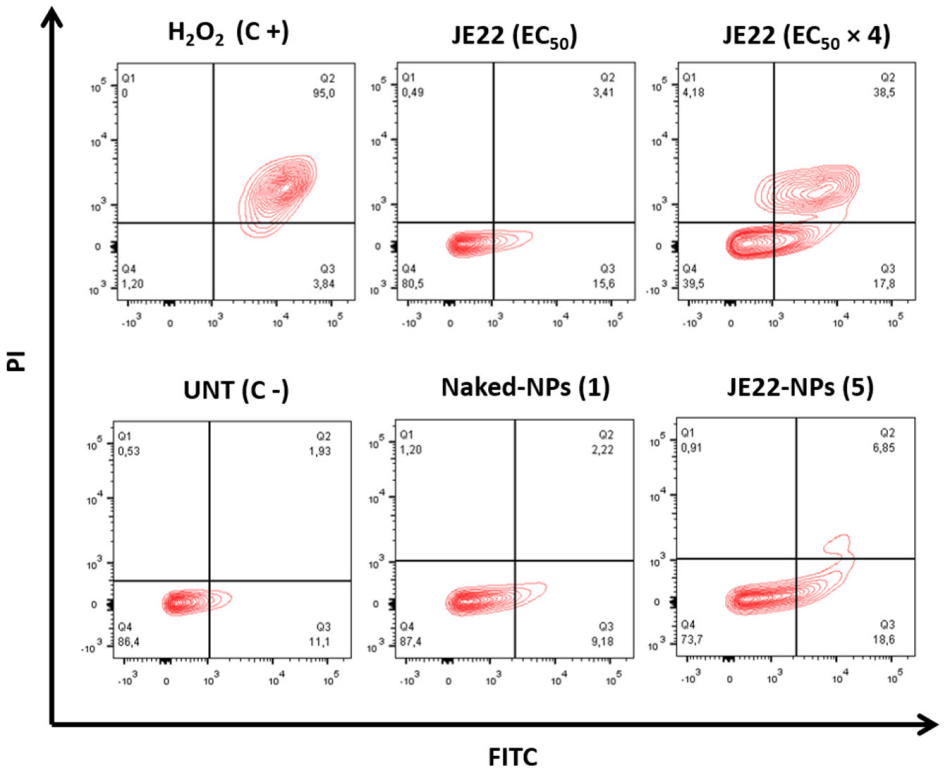


**Figure 9.** Effect of **JE22** and **JE22-NPs** (**5**) on MDA-MB-231 cell apoptosis. Representative scatter plots of PI (*y*-axis) versus FITC (*x*-axis) of cells after treatment with **JE22-NPs** (**5**) (20,000 NPs/cell), **JE22** ($EC_{50}$ and 4 × $EC_{50}$), and **Naked-NPs** (**1**) (20,000 NPs/cell) for 24 h. Number of nanoparticles was determined by spectrophotometric analysis (see Figure S7). The cells were analyzed after double staining with Annexin V-FITC/PI by flow cytometry. Dot plots of $H_2O_2$ (2 mM, treatment of 4 h) and untreated cells were represented as the positive and negative control, respectively. Q1-4 quadrants represent necrotic (Annexin V-FITC-, PI+), late (Annexin V-FITC+, PI+), and early (Annexin V-FITC+, PI-) apoptotic and viable (Annexin V-FITC-, PI-) cells, respectively.

## 4. Conclusions

In this work, we successfully designed and evaluated an innovative nanodevice for selective anticancer therapy targeting CD44 receptors. In particular, a ketone derivative of THIQ (**JE22**) to target the CD44 HABD was synthetized and conjugated to polymeric nanoparticles via hydrazone bond to achieve a nanodevice for selective release in tumor microenvironments. Computational analysis confirmed that the designed THIQ ketone

derivative (**JE22**) is a good candidate to interact with the CD44 receptor. Remarkably, the conjugation of this CD44 inhibitor to the nanodevice **JE22-NPs** (**5**) achieved more than 150-fold reduction of the dosis required to render a significant therapeutic effect. It was determined that the pH-sensitive strategy to release the CD44 inhibitor from the nanodevice at the acidic tumor microenviroment enhanced the efficient interaction with the CD44 receptor and significantly reduced HA binding. The migration of CD44+ cells decreased, and a non-significant apoptotic effect was observed following treatment with **JE22-NPs** (**5**). Additionally, the nanodevide was selective to cancerous CD44+ cells and safe to non-cancerous cells.

Based on this preliminary investigation, further studies will be undertaken to characterise the interaction between this THIQ derivative and the CD44 HA binding domain to design a next generation of CD44 targeted nanotherapies.

**Supplementary Materials:** The following supporting information can be downloaded at: https://www.mdpi.com/article/10.3390/pharmaceutics14040788/s1, Scheme S1. Chemical structures of the THIQ-ester and **JE22** ligands with the nomenclature used in the CHARMM force field parameterization. Table S1. CHARMM force field parameterization of **THIQ-ester**. Table S2. CHARMM force field parameterization of **JE22**. Table S3. CHARMM force field parameterization of **THIQ-ester**. Table S4. CHARMM force field parameterization of **JE22**. Table S5. CHARMM force field parameterization of **THIQ-ester**. Table S6. CHARMM force field parameterization of **JE22**. Table S7. CHARMM force field parameterization of **THIQ-ester**. Table S8. CHARMM force field parameterization of **JE22**. Table S9. Code, name, and structure of synthesized nanoparticles. Figure S1. Comparison of the potential energy surface (PES) from quantum mechanics calculations (QM) in black and the fitted torsions in red for some the torsional angles of (A) **JE22** and (B) optimized **THIQ-ester**. Figure S2. Evolution of the Cα root-mean-square deviation (RMSD) of different structural elements of CD44 from the initial structure as a function of time for the system with (A) **JE22** or (B) **THIQ-ester**. Figure S3. Evolution in time of the minimum distance between any atom of the ligand, either (A) **JE22** or (B) **THIQ-ester**, and any atom of the binding site composed by N29 T31 E41 R80 C81 R82 R155, for each of the five replicas. Figure S4. Normalized probability density of the Cα RMSD. Figure S5. $^{1}$H NMR **JE22**. Figure S6. $^{13}$C NMR **JE22**. Figure S7. Calibration standard curve of concentration of nanoparticles (OD 600). Figure S8. DLS analysis of **JE22-NPs** (**5**) before and after incubation in PBS pH = 5 for 5 days. Figure S9. Bar graph showing the zeta potential (mV) values of **JE22-NPs** (**5**). Figure S10. (A) Spectrophotometry determination of selected wavelength of **JE22**. (B) Calibration standard curve of **JE22** obtained by spectrophotometry. (C) Calibration curve of **JE22** acquired by HPLC. Figure S11. Flow cytometry analysis of the expression of CD44 in MDA-MB-231 and MCF-7 cells. Figure S12. Bar graph showing the effect of **JE22-NPs** (**5**) on cell viability of MCF-7 cell line. Figure S13. MDA-MB-231 cell viability after treatment with **JE22-NPs** (**5**) ($EC_{50}$ and $EC_{50} \times 2$) preincubated with anti-CD44 antibody. Figure S14. Dose–response curve (percentage of cell viability versus concentration) of MDA-MB-231 after treatment with **JE22-NPs** (**5**), expressed in NPs/cell. Figure S15. Viability of MDA-MB-231 cells incubated for 1.5, 3, and 6 h with DMEM media at pH = 5. Figure S16. Bar graph showing the effect of **JE22-NPs** (**5**) on cell viability of HEK-293 cell line. Figure S17. Confocal microscopy orthogonal (xy, xz, and yz) view representing the planes of intersection at the position of green cross line. The maximum intensity projection of the z-stack is shown blue for nuclei (DAPI), green for anti-human CD44 (FITC), and red for **JE22-NPs** (**5**) (APC). Figure S18. Effect of **JE22-NPs** (**5**) on MCF-7 cell apoptosis. References of the supplementary materials. References [17,30,36,48–55] are cited in the Supplementary Materials.

**Author Contributions:** Methodology, investigation, and validation, J.M.E.-R., B.R.-R., V.C.-C. and S.G.-R.; writing—original draft preparation, J.M.E.-R., B.R.-R., V.C.-C., S.G.-R., C.D., O.C.-L., A.C.-G. and R.M.S.-M.; writing—review and editing, funding acquisition, supervision, and conceptualization, C.D., O.C.-L., A.C.-G. and R.M.S.-M. All authors have read and agreed to the published version of the manuscript.

**Funding:** This research was funded by the Consejería de Economía, Conocimiento, Empresas y Universidad of the Junta de Andalucía (grant number Excellence Research Project P18-RT-1679) and the Research Results Transfer Office (OTRI) of the University of Granada (grant number PR/17/006 project). This work was partially supported by grants from the Spanish Ministry of Economy and Competitiveness (MINECO), grant number PID2019.110987RB.I00; the Health Institute Carlos III (ISCIII), grant number DTS18/00121 the Junta de Andalucía-FEDER, Ministry of Economy, Knowledge, Companies, and University (FEDER 2018: ref. B-FQM-475-UGR18, PAIDI2020: ref. PT18-TP-4160); and the Andalusian Regional Government, grant number PAIDI-TC-PVT-PSETC-2.0. C.D. thanks HECBioSim, the UK High End Computing Consortium for Biomolecular Simulation (hecbiosim.ac.uk), which is supported by the EPSRC (EP/L000253/1) for awarding computing time in Jade, a UK Tier-2 resource. B.R.-R. gratefully acknowledges funding from the European Union's Horizon 2020 Research and Innovation Program under Marie Sklodowska-Curie Grant Agreement no. 754446 and UGR Research and Knowledge Transfer Fund—Athenea3i. J.M.E.-R. thanks the Spanish Ministry of Education for PhD funding (scholarship FPU 16/02061). V.C.-C. thanks the Andalusian Regional Government for her postdoctoral fellowship (POSTDOC_21_00118).

**Institutional Review Board Statement:** Not applicable.

**Informed Consent Statement:** Not applicable.

**Data Availability Statement:** The data that support the findings of this study are freely available on request from the corresponding author.

**Acknowledgments:** The authors thank the technical support of the Microscopy and Molecular Image Unit and Flow Cytometry from GENYO. The authors thank the technical support of the Mass Spectrometry and Chromatography Unit of the Scientific Instrumentation Center of the University of Granada, in particular to Samuel Cantarero. The authors are members of the network NANOCARE (RED2018-102469-T) funded by the STATE INVESTIGATION AGENCY. Graphical abstract and Figure 1 has been created with BioRender.com (accessed on 5 March 2022).

**Conflicts of Interest:** The authors declare no conflict of interest.

## References

1. Fraser, J.R.; Laurent, T.C.; Laurent, U.B. Hyaluronan: Its nature, distribution, functions and turnover. *J. Intern. Med.* **1997**, *242*, 27–33. [CrossRef] [PubMed]
2. Toole, B.P. Hyaluronan: From extracellular glue to pericellular cue. *Nat. Rev. Cancer* **2004**, *4*, 528–539. [CrossRef] [PubMed]
3. Fallacara, A.; Baldini, E.; Manfredini, S.; Vertuani, S. Hyaluronic Acid in the Third Millennium. *Polymers* **2018**, *10*, 701. [CrossRef]
4. Karousou, E.; Misra, S.; Ghatak, S.; Dobra, K.; Götte, M.; Vigetti, D.; Passi, A.; Karamanos, N.K.; Skandalis, S.S. Roles and targeting of the HAS/hyaluronan/CD44 molecular system in cancer. *Matrix Biol.* **2017**, *59*, 3–22.
5. Chanmee, T.; Ontong, P.; Itano, N. Hyaluronan: A modulator of the tumor microenvironment. *Cancer Lett.* **2016**, *375*, 20–30. [CrossRef]
6. Misra, S.; Heldin, P.; Hascall, V.C.; Karamanos, N.K.; Skandalis, S.S.; Markwald, R.R.; Ghatak, S. Hyaluronan-CD44 interactions as potential targets for cancer therapy. *FEBS J.* **2011**, *278*, 1429–1443.
7. Senbanjo, L.T.; Chellaiah, M.A. CD44: A multifunctional cell surface adhesion receptor is a regulator of progression and metastasis of cancer cells. *Front. Cell Dev. Biol.* **2017**, *5*, 18. [CrossRef]
8. Shi, J.; Kantoff, P.W.; Wooster, R.; Farokhzad, O.C. Cancer nanomedicine: Progress, challenges and opportunities. *Nat. Rev. Cancer* **2017**, *17*, 20–37. [CrossRef]
9. Germain, M.; Caputo, F.; Metcalfe, S.; Tosi, G.; Spring, K.; Åslund, A.; Pottier, A.; Schiffelers, R.; Ceccaldi, A.; Schmid, R. Delivering the power of nanomedicine to patients today. *J. Control. Release* **2020**, *326*, 164–171. [CrossRef]
10. Chiesa, E.; Greco, A.; Riva, F.; Dorati, R.; Conti, B.; Modena, T.; Genta, I. Hyaluronic Acid-Based Nanoparticles for Protein Delivery: Systematic Examination of Microfluidic Production Conditions. *Pharmaceutics* **2021**, *13*, 1565.
11. Liang, X.; Li, X.; Duan, J.; Chen, Y.; Wang, X.; Pang, L.; Kong, D.; Song, B.; Li, C.; Yang, J. Nanoparticles with CD44 Targeting and ROS Triggering Properties as Effective in Vivo Antigen Delivery System. *Mol. Pharm.* **2018**, *15*, 508–518. [CrossRef] [PubMed]
12. Gaio, E.; Conte, C.; Esposito, D.; Reddi, E.; Quaglia, F.; Moret, F. CD44 Targeting Mediated by Polymeric Nanoparticles and Combination of Chlorine TPCS2a-PDT and Docetaxel-Chemotherapy for Efficient Killing of Breast Differentiated and Stem Cancer Cells In Vitro. *Cancers* **2020**, *12*, 278. [CrossRef]
13. Shi, J.; Ren, Y.; Ma, J.; Luo, X.; Li, J.; Wu, Y.; Gu, H.; Fu, C.; Cao, Z.; Zhang, J. Novel CD44-targeting and pH/redox-dual-stimuli-responsive core–shell nanoparticles loading triptolide combats breast cancer growth and lung metastasis. *J. Nanobiotechnol.* **2021**, *19*, 188. [CrossRef]

14. Navarro-Marchal, S.A.; Griñán-Lisón, C.; Entrena, J.M.; Ruiz-Alcalá, G.; Tristán-Manzano, M.; Martin, F.; Pérez-Victoria, I.; Peula-García, J.M.; Marchal, J.A. Anti-CD44-Conjugated Olive Oil Liquid Nanocapsules for Targeting Pancreatic Cancer Stem Cells. *Biomacromolecules* **2021**, *22*, 1374–1388. [CrossRef] [PubMed]
15. Banerji, S.; Wright, A.J.; Noble, M.; Mahoney, D.J.; Campbell, I.D.; Day, A.J.; Jackson, D.G. Structures of the Cd44-hyaluronan complex provide insight into a fundamental carbohydrate-protein interaction. *Nat. Struct. Mol. Biol.* **2007**, *14*, 234–239. [CrossRef]
16. Liu, L.K.; Finzel, B.C. Fragment-based identification of an inducible binding site on cell surface receptor CD44 for the design of protein-carbohydrate interaction inhibitors. *J. Med. Chem.* **2014**, *57*, 2714–2725. [CrossRef] [PubMed]
17. Unciti-Broceta, A.; Johansson, E.; Yusop, R.M.; Sánchez-Martín, R.M.; Bradley, M. Synthesis of polystyrene microspheres and functionalization with Pd0 nanoparticles to perform bioorthogonal organometallic chemistry in living cells. *Nat. Protoc.* **2012**, *7*, 1207–1218. [CrossRef]
18. Altea-Manzano, P.; Unciti-Broceta, J.D.; Cano-Cortes, V.; Ruiz-Blas, M.P.; Valero-Griñan, T.; Diaz-Mochon, J.J.; Sanchez-Martin, R. Tracking cell proliferation using a nanotechnology-based approach. *Nanomedicine* **2017**, *12*, 1591–1605. [CrossRef] [PubMed]
19. Valero, T.; Delgado-González, A.; Unciti-Broceta, J.D.; Cano-Cortés, V.; Pérez-López, A.M.; Unciti-Broceta, A.; Sánchez Martín, R.M. Drug "Clicking" on Cell-Penetrating Fluorescent Nanoparticles for *In Cellulo* Chemical Proteomics. *Bioconjug. Chem.* **2018**, *29*, 3154–3160.
20. Cano-Cortes, M.V.; Navarro-Marchal, S.A.; Ruiz-Blas, M.P.; Diaz-Mochon, J.J.; Marchal, J.A.; Sanchez-Martin, R.M. A Versatile Theranostic Nanodevice Based on an Orthogonal Bioconjugation Strategy for Efficient Targeted Treatment and Monitoring of Triple Negative Breast Cancer. *Nanomed. Nanotechnol. Biol. Med.* **2020**, *24*, 102120. [CrossRef] [PubMed]
21. Cano-Cortes, M.V.; Laz-Ruiz, J.A.; Diaz-Mochon, J.J.; Sanchez-Martin, R.M. Characterization and Therapeutic Effect of a pH Stimuli Responsive Polymeric Nanoformulation for Controlled Drug Release. *Polymers* **2020**, *12*, 1265. [CrossRef] [PubMed]
22. Cano-Cortes, M.V.; Altea-Manzano, P.; Laz-Ruiz, J.A.; Unciti-Broceta, J.D.; Lopez-Delgado, F.J.; Espejo-Roman, J.M.; Diaz-Mochon, J.J.; Sanchez-Martin, R.M. An effective polymeric nanocarrier that allows for active targeting and selective drug delivery in cell coculture systems. *Nanoscale* **2021**, *13*, 3500–3511. [CrossRef] [PubMed]
23. Jo, S.; Klauda, J.B.; Im, W. CHARMM-GUI Membrane Builder for Mixed Bilayers and Its Application to Yeast Membranes. *Biophys. J.* **2009**, *96*, 41a. [CrossRef]
24. Kumar, R.; Iyer, V.G.; Im, W. CHARMM-GUI: A graphical user interface for the CHARMM users. *Abstr. Pap. Am. Chem. S.* **2007**, *233*, 273.
25. Lee, J.; Cheng, X.; Swails, J.M.; Yeom, M.S.; Eastman, P.K.; Lemkul, J.A.; Wei, S.; Buckner, J.; Jeong, J.C.; Qi, Y.F.; et al. CHARMM-GUI Input Generator for NAMD, GROMACS, AMBER, OpenMM, and CHARMM/OpenMM Simulations Using the CHARMM36 Additive Force Field. *J. Chem. Theory Comput.* **2016**, *12*, 405–413. [CrossRef] [PubMed]
26. Wu, E.L.; Cheng, X.; Jo, S.; Rui, H.; Song, K.C.; Davila-Contreras, E.M.; Qi, Y.F.; Lee, J.M.; Monje-Galvan, V.; Venable, R.M.; et al. CHARMM-GUI Membrane Builder Toward Realistic Biological Membrane Simulations. *J. Comput. Chem.* **2014**, *35*, 1997–2004. [CrossRef]
27. MacKerell, A.D.; Bashford, D.; Bellott, M.; Dunbrack, R.L.; Evanseck, J.D.; Field, M.J.; Fischer, S.; Gao, J.; Guo, H.; Ha, S.; et al. All-atom empirical potential for molecular modeling and dynamics studies of proteins. *J. Phys. Chem. B* **1998**, *102*, 3586–3616. [CrossRef] [PubMed]
28. Huang, J.; MacKerell, A.D. CHARMM36 all-atom additive protein force field: Validation based on comparison to NMR data. *J. Comput. Chem.* **2013**, *34*, 2135–2145. [CrossRef]
29. Jorgensen, W.L.; Chandrasekhar, J.; Madura, J.D.; Impey, R.W.; Klein, M.L. Comparison of Simple Potential Functions for Simulating Liquid Water. *J. Chem. Phys.* **1983**, *79*, 926–935. [CrossRef]
30. Kim, S.; Lee, J.; Jo, S.; Brooks, C.L.; Lee, H.S.; Im, W. CHARMM-GUI ligand reader and modeler for CHARMM force field generation of small molecules. *J. Comput. Chem.* **2017**, *38*, 1879–1886. [CrossRef]
31. Kim, S.; Lee, J.; Jo, S.; Im, W. CHARMM-GUI Ligand Reader & Modeler. *Biophys. J.* **2017**, *112*, 289a.
32. Vanommeslaeghe, K.; Hatcher, E.; Acharya, C.; Kundu, S.; Zhong, S.; Shim, J.; Darian, E.; Guvench, O.; Lopes, P.; Vorobyov, I.; et al. CHARMM General Force Field: A Force Field for Drug-Like Molecules Compatible with the CHARMM All-Atom Additive Biological Force Fields. *J. Comput. Chem.* **2010**, *31*, 671–690. [CrossRef] [PubMed]
33. Frisch, M.J.; Trucks, G.W.; Schlegel, H.B.; Scuseria, G.E.; Robb, M.A.; Cheeseman, J.R.; Scalmani, G.; Barone, V.; Petersson, G.A.; Nakatsuji, H.; et al. *Gaussian 16 Rev. C.01*; Gaussian Inc.: Wallingford, CT, USA, 2016.
34. Jones, K.; Karier, P.; Klussmann, M. C1-substituted N-alkyl tetrahydroisoquinoline derivatives through V-catalyzed oxidative coupling. *ChemCatChem* **2012**, *4*, 51–54. [CrossRef]
35. Manchun, S.; Dass, C.R.; Sriamornsak, P. Targeted Therapy for Cancer Using Ph-Responsive Nanocarrier Systems. *Life Sci.* **2012**, *90*, 381–387. [CrossRef]
36. Unciti-Broceta, J.D.; Cano-Cortés, V.; Altea-Manzano, P.; Pernagallo, S.; Díaz-Mochón, J.J.; Sánchez-Martín, R.M. Number of nanoparticles per cell through a spectrophotometric method—A key parameter to assess nanoparticle-based cellular assays. *Sci. Rep.* **2015**, *5*, 10091. [CrossRef]
37. Pietrovito, L.; Cano-Cortés, V.; Gamberi, T.; Magherini, F.; Bianchi, L.; Bini, L.; Sánchez-Martín, R.M.; Fasano, M.; Modesti, A. Cellular response to empty and palladium-conjugated amino-polystyrene nanospheres uptake: A proteomic study. *Proteomics* **2015**, *15*, 34–43. [CrossRef] [PubMed]

38. O'Brien, J.; Wilson, I.; Orton, T.; Pognan, F. Investigation of the Alamar Blue (resazurin) fluorescent dye for the assessment of mammalian cell cytotoxicity. *Eur. J. Biochem.* **2000**, *267*, 5421–5426. [CrossRef] [PubMed]
39. Olsson, E.; Honeth, G.; Bendahl, P.; Saal, L.H.; Gruvberger-Saal, S.; Ringnér, M.; Vallon-Christersson, J.; Jönsson, G.; Holm, K.; Lövgren, K.; et al. CD44 isoforms are heterogeneously expressed in breast cancer and correlate with tumor subtypes and cancer stem cell markers. *BMC Cancer* **2011**, *11*, 418. [CrossRef] [PubMed]
40. Sheridan, C.; Kishimoto, H.; Fuchs, R.K.; Fuchs, R.K.; Mehrotra, S.; Bhat-Nakshatri, P.; Turner, C.H.; Goulet, R.J.; Badve, S.; Nakshatri, H. CD44+/CD24-breast cancer cells exhibit enhanced invasive properties: An early step necessary for metastasis. *Breast Cancer Res.* **2006**, *8*, R59. [CrossRef] [PubMed]
41. Michl, J.; Kyung, C.K.; Swietach, P. Evidence-based guidelines for controlling pH in mammalian live-cell culture systems. *Commun. Biol.* **2019**, *2*, 144. [CrossRef]
42. Ali, H.; Al-Yatama, M.K.; Abu-Farha, M.; Behbehani, K.; Al Madhoun, A. Multi-lineage differentiation of human umbilical cord Wharton's Jelly Mesenchymal Stromal Cells mediates changes in the expression profile of stemness markers. *PLoS ONE* **2015**, *10*, e0122465. [CrossRef] [PubMed]
43. Bhattacharya, D.; Svechkarev, D.; Souchek, J.; Hill, T.; Taylor, M.; Natarajan, A.; Mohs, A. Impact of structurally modifying hyaluronic acid on CD44 interaction. *J. Mater. Chem. B* **2017**, *5*, 8183–8192. [CrossRef]
44. Ponta, H.; Sherman, L.; Herrlich, P.A. CD44: From adhesion molecules to signalling regulators. *Nat. Rev. Mol. Cell Biol.* **2003**, *4*, 33–45. [CrossRef]
45. Aguirre-Alvarado, C.; Segura-Cabrera, A.; Velázquez-Quesada, I.; Hernández-Esquivel, M.A.; García-Pérez, C.A.; Guerrero-Rodríguez, S.L.; Ruiz-Moreno, A.G.; Rodríguez-Moreno, A.; Pérez-Tapia, S.-M.; Velasco-Velázquez, M.A. Virtual screening-driven repositioning of etoposide as CD44 antagonist in breast cancer cells. *Oncotarget* **2016**, *7*, 23772–23784. [CrossRef]
46. Tsujimoto, Y.; Shimizu, S. Role of the mitochondrial membrane permeability transition in cell death. *Apoptosis* **2007**, *5*, 835–840. [CrossRef] [PubMed]
47. Zhong, Z.F.; Tan, W.; Tian, K.; Yu, H.; Qiang, W.A.; Wang, Y.T. Combined effects of furanodiene and doxorubicin on the migration and invasion of MDA-MB-231 breast cancer cells in vitro. *Oncol. Rep.* **2017**, *37*, 2016–2024. [CrossRef]
48. Essmann, U.; Perera, L.; Berkowitz, M.L.; Darden, T.; Lee, H.; Pedersen, L.G. A smooth particle mesh Ewald method. *J. Chem. Phys.* **1995**, *103*, 8577–8593. [CrossRef]
49. Verlet, L. Computer "Experiments" on Classical Fluids. I. Thermodynamical Properties of Lennard−Jones Molecules. *Phys. Rev.* **1967**, *159*, 98–103. [CrossRef]
50. Feller, S.E.; Zhang, Y.; Pastor, R.W.; Brooks, B.R. Constant pressure molecular dynamics simulation: The Langevin piston method. *J. Chem. Phys.* **1995**, *103*, 4613–4621. [CrossRef]
51. Miyamoto, S.; Kollman, P.A. SETTLE−an analytical version of the Shake and Rattle algorithm for rigid water models. *J. Comput. Chem.* **1992**, *13*, 952–962. [CrossRef]
52. Tuckerman, M.; Berne, B.J.; Martyna, G.J. Reversible Multiple Time Scale Molecular−Dynamics. *J. Chem. Phys.* **1992**, *97*, 1990–2001. [CrossRef]
53. Phillips, J.C.; Braun, R.; Wang, W.; Gumbart, J.; Tajkhorshid, E.; Villa, E.; Chipot, C.; Skeel, R.D.; Kale, L.; Schulten, K. Scalable molecular dynamics with NAMD. *J. Comput. Chem.* **2005**, *26*, 1781–1802. [CrossRef]
54. Phillips, J.C.; Hardy, D.J.; Maia, J.D.C.; Stone, J.E.; Ribeiro, J.V.; Bernardi, R.C.; Buch, R.; Fiorin, G.; Henin, J.; Jiang, W.; et al. Scalable molecular dynamics on CPU and GPU architectures with NAMD. *J. Chem. Phys.* **2020**, *153*, 044130. [CrossRef] [PubMed]
55. Alexander, L.; Sánchez−Martín, R.; Bradley, M. Knocking (Anti)−Sense into Cells: The Microsphere Approach to Gene Silencing. *Bioconjug. Chem.* **2009**, *20*, 422–426. [CrossRef] [PubMed]